




Spectral Index Distribution of Various Scale Components in Supernova Remnant Cassiopeia A

Xianhuan Lei^{1,2}, Hui Zhu¹, Zongyao Yin³ , Haiyan Zhang^{1,2}, Wenwu Tian^{1,2}, and Xianchuan Yu³

¹ Key Laboratory of Radio Astronomy and Technology, National Astronomical Observatories, Chinese Academy of Sciences, Beijing 100101, China; zhuhui@bao.ac.cn

² University of Chinese Academy of Sciences, Beijing 101408, China; hyzhang@nao.cas.cn, tw@bao.ac.cn

³ School of Artificial Intelligence, Beijing Normal University, Beijing 100875, China

Received 2024 March 15; revised 2024 April 3; accepted 2024 April 8; published 2024 May 13

Abstract

Cassiopeia A (Cas A) is a well-known candidate for studying cosmic-ray acceleration, in which compact features of various scales have attracted much attention. Based on observations by the Very Large Array of Cas A at 6 cm and 21 cm, we measure the spectral index distribution of various scale components using the observation of the 1998 epoch. We decompose its total density image into nine scale components, and map the temperature spectral index distribution of each component, which ranges from -2.48 ± 0.01 to -2.91 ± 0.05 . We find that the spectral indices increase from the small scale to large scale components. A damped post-shock magnetic field model with a strength larger than $\sim 200 \mu\text{G}$ and a damping length scale less than $\sim 10\%$ of the remnant radius can account for the spectral index variation naturally.

Key words: ISM: supernova remnants – (ISM:) cosmic rays – radio continuum: ISM

1. Introduction

Supernova remnants (SNRs) are widely considered as the primary source of Galactic Cosmic Ray (CR) acceleration (Blasi 2013; Brose et al. 2022; Vink & Bamba 2022), where high-energy particles can be accelerated to TeV or even PeV energy level through the diffusion shock acceleration (DSA) mechanism (Bell 1978; Blandford & Eichler 1987; Tian et al. 2008; Cao et al. 2021). Although there is still a lack of PeV particles in SNRs, the characteristic π^0 -decay feature, detected in the gamma-ray SNRs IC 443, W44 and W51C, shows that SNRs indeed can accelerate cosmic-ray protons to relativistic energy (Ackermann et al. 2013; Cardillo et al. 2014; Jogler & Funk 2016).

Cassiopeia A (Cas A), as the youngest known core-collapse SNR with an age of ~ 350 yr in the Galaxy (Fesen et al. 2006), has long been considered as one of the powerful accelerators that can accelerate relativistic particles to PeV energy level. The optical spectrum of its light echo indicates that the remnant originated from a Type IIb supernova explosion (Krause et al. 2008). Based on its explosion date, Reed et al. (1995) combined radial velocity and proper motion of optical filaments to yield its distance of ~ 3.4 kpc. As a radio bright source, most of its bright radio emission comes from a radio ring with a radius of ~ 1.7 pc that marks the location of ejecta interacting with the reverse shock (Kassim et al. 1995; Morse et al. 2004), and the fainter radio emission mainly comes from a plateau region extending to a radius of ~ 2.5 pc (DeLaney et al. 2014). Non-thermal X-ray emission has been detected both in forward

and reverse shocks, and dominant non-thermal X-ray emission is associated with filaments or knots in the reverse-shock region (Gotthelf et al. 2001; Helder & Vink 2008). Thanks to the HERGA stereoscopic Cherenkov telescope system, Cas A was the first SNR with confirmed TeV gamma-ray emission (Aharonian et al. 2001), which was further verified by MAGIC (Albert et al. 2007) and VERITAS (Humensky 2008).

SNRs are well-established non-thermal radio sources, i.e. $S_\nu \propto \nu^\alpha$, with an overall spectral index of about -0.5 (Green 2019). Cas A with an overall mean spectral index of -0.77 is obviously steeper (Baars et al. 1977), which has been considered as the result of nonlinear DSA effects (Domček et al. 2021). Bright knots in Cas A are the interesting targets of most studies, and the spectral index of these knots varies from -0.64 to -0.92 (Anderson et al. 1991; Anderson & Rudnick 1996). In contrast, the features outside the bright ring have steeper spectral index (Wright et al. 1999).

In this letter, we analyze the spectral index distribution of various scale components in Cas A using the constrained diffusion decomposition (CDD) method. Spectral index data calculated here are based on the high-resolution observations of Very Large Array (VLA⁴) for Cas A at 1.475 GHz (21 cm) and 4.747 GHz (6 cm). Section 2 describes the data calibration process and the method of multi-scale decomposition images. Section 3 lists the spectral index measurement results of each scale component. The work concludes in Section 4.

⁴ <https://science.nrao.edu/facilities/vla>

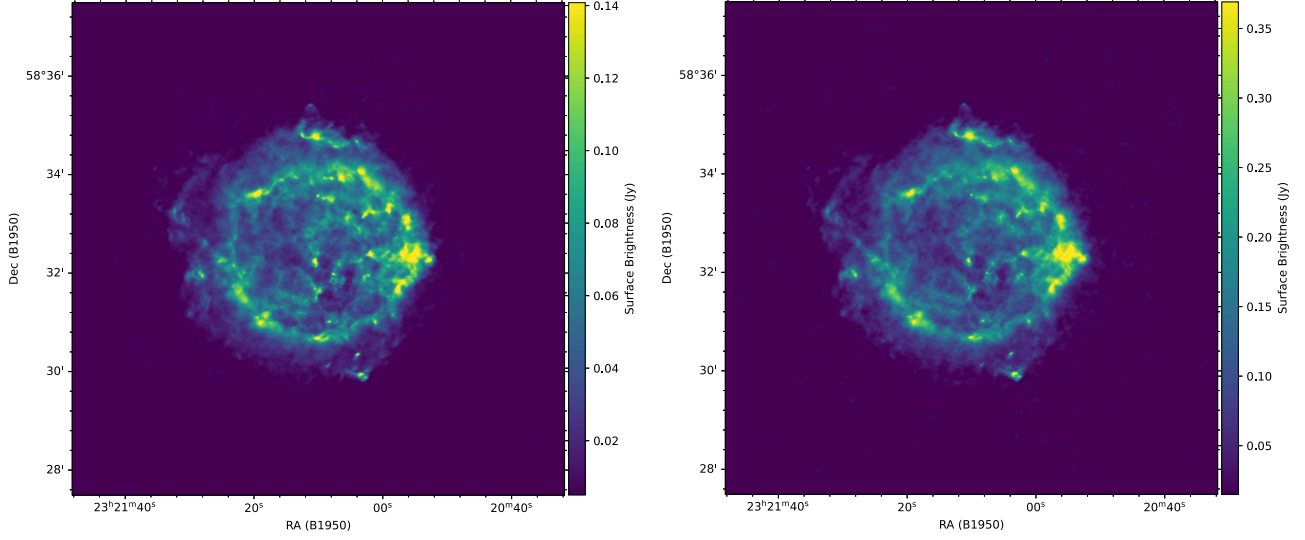


Figure 1. Total density image of Cas A at 4.747 GHz (left) and 1.475 GHz (right) from epoch 1998 observed by VLA; the angular resolution is $2''.0$. Color-scale is in units of Jy beam^{-1} .

2. Data and Image Decomposition

Since the VLA commissioning in 1980, Cas A has been widely observed at multiple frequencies. Based on the high-resolution observations of VLA, the evolution of compact knots within Cas A have been well-studied (Anderson & Rudnick 1995; Lei et al. 2022). To understand the spectral index distribution of various scale features in Cas A, we follow the CDD method developed by Li (2022) to decompose the total density images of the SNR into various angular scale components.

2.1. Data Reduction

In this work, we used images of 6 cm and 21 cm obtained by VLA in 1997–1998 (Project code: AR0378) to construct the spectral index distribution maps of Cas A. The two images were observed by the *A*-, *B*-, *C*- and *D*-configurations of VLA, where the *A*-configuration is the most extended with a maximum baseline of 36.4 km, and the *D*-configuration is the most compact with a minimum baseline of 0.035 km.⁵ To improve the aperture coverage, observations were made at several frequencies around 4.747 GHz (4.410, 4.985, 4.640 and 5.085 GHz) and 1.475 GHz (1.285, 1.464, 1.365 and 1.665 GHz).

The data calibrations were performed by the Common Astronomy Software Applications (CASA; McMullin et al. 2007) package. Primary flux calibration was based on 0134+329 (3C 48), and the phase calibrator was 2352+495. To match the resolution of the 21 cm image, the data of *A*-configuration at 6 cm have been excluded. After initial

calibration, we performed multiple self-calibration and imaging to clean the residual calibration artifacts. A Multi-Scale CLEAN (MS) deconvolution method was used for imaging (Cornwell 2008), which avoids a negative “bowl” around the source. During the imaging, the used multiscale was $0'', 2''.5, 25'', 75''$ and $150''$, and “briggs” weighting with a parameter $\text{robust} = 0$. The resulting total flux density images are shown in Figure 1.

The radio flux density of Cas A described by the spectrum between 0.3 and 31 GHz at the epoch 1980.0 is given

$$\log S = 5.745 - 0.77 \log \nu, \quad (1)$$

where S is in Jy and ν is in MHz (Baars et al. 1977). With a fade rate of $0.67\% \text{ yr}^{-1}$ reported by Trotter et al. (2017), the calculated absolute flux density at epoch 1998.0 is $S_{4.747 \text{ GHz}} = 728.65 \text{ Jy}$ and $S_{1.475 \text{ GHz}} = 1792.58 \text{ Jy}$. The integrated flux density of our calibrated images is $S_{4.747 \text{ GHz}} = 748.61 \pm 37 \text{ Jy}$ and $S_{1.475 \text{ GHz}} = 1858.60 \pm 93 \text{ Jy}$, and the uncertainty is based on 5% absolute accuracy of the spectral flux density estimated by 1977 Baars et al. (1977).

The minimum separation of the radio telescope is 35 m, which results in an unsampled aperture plane within a diameter $\lambda/2D_{\min}$ being $\sim 170''$ at 6 cm and $\sim 600''$ at 21 cm. Since the diameter of Cas A is $\sim 300''$, the sampling of the large scale structure in the remnant is very different between 6 cm and 21 cm. To explore the effect of sampling difference for imaging, we have removed baseline data of less than 140 m from the 21 cm data to ensure that the aperture plane diameter is consistent with the 6 cm data. The flux density of the image is consistent with maintaining short baselines. Therefore, the sampling difference does not affect the spectral index calculation.

⁵ <https://science.nrao.edu/facilities/vla/docs/manuals/oss/performance>

Table 1
Brightness Spectral Index of Each Component for Cas A, $\lambda = 6$ cm and 21 cm

Scale (")	[1.0–3.0] [25.0–38.0]	[3.0–5.0] [38.0–53.0]	[5.0–10.0] [53.0–68.0]	[10.0–15.0] [> 68.0]	[15.0–25.0]
$S_{6\text{ cm}}$ (Jy)	59.79 71.03	51.03 65.72	93.93 53.25	61.03 205.95	80.05
$S_{21\text{ cm}}$ (Jy)	105.49 197.55	101.64 189.10	219.54 150.83	149.97 537.85	204.45
α	-0.49 ± 0.01 -0.88 ± 0.02	-0.59 ± 0.01 -0.90 ± 0.02	-0.73 ± 0.02 -0.89 ± 0.02	-0.77 ± 0.02 -0.82 ± 0.02	-0.80 ± 0.02

2.2. Multi-scale Maps

Cas A, a shell-type SNR, contains various angular size structures, and these features are widely used to study the relationship between the dynamical evolution and charged particle energy distributions. We decompose the total-density images observed by VLA in 6 cm and 21 cm into different scale components using the CDD method. Referring to the wavelet transform method, Li (2022) developed the CDD method, which eliminates an artifact that appears in other decomposition methods.

In the CDD method, an input image $I(x, y)$ is convolved with a set of nonlinear constraint diffusion equations of increasing scales to construct a set of corresponding smoothed images $I_l(x, y)$, and the smoothed images are subtracted from each other to produce decomposed images. The scale of each component is $n = 0$: [1.0–3.0] arcsec, $n = 1$: [3.0–5.0] arcsec, $n = 2$: [5.0–10.0] arcsec, $n = 3$: [10.0–15.0] arcsec, $n = 4$: [15.0–25.0] arcsec, $n = 5$: [25.0–38.0] arcsec, $n = 6$: [38.0–53.0] arcsec, $n = 7$: [53.0–68.0] arcsec, $n = 8$: [>68.0] arcsec. Flux density and spectral index of each component are presented in Table 1, and the errors of spectral index are calculated based on an accuracy of 2% (Baars et al. 1977). Taking the C-band image as an example, the images of each scale component are listed in Figure 2. The components $n = 0$ –5 are predominantly the bright compact features and fragments. The diffuse plateau regions are expressed with components $n = 7$ and 8.

3. Results and Discussion

We analyze the temperature spectral index β between L - and C-band of each component based on the temperature-versus-temperature plots (T-T plots) method (Turtle et al. 1962), which is defined as $T_\nu \propto \nu^\beta$ and related to the flux density spectral index α by $\beta = \alpha - 2$. The T-T plot method is performed by linearly fitting the brightness temperature T_1 at frequency ν_1 to the bright temperature T_2 at frequency ν_2 , and the temperature spectral index β is obtained from the slope of the line. The T-T plots of each component between frequency 1.475 and 4.745 GHz are shown in Figure 3, with the radio spectral index variations in a range of -0.48 ± 0.01 to -0.91 ± 0.05 . When we simply consider Cas A as a single

structure model, the calculated mean spectral index of the whole remnant is $\alpha = -0.78 \pm 0.02$, which coincides with the result of Baars et al. (1977).

For the complex morphology and wide range spectral index distribution of Cas A, Atoyan et al. (2000b) developed a two-zone model to explain the detailed spectral properties. Combined with the spectral index distribution of radio knots calculated in Anderson & Rudnick (1996), the two-zone model places compact components and steep-spectrum radio knots at zone 1, and the other diffusion region with electron densities relatively lower is zone 2. The definitions of these two zones indicate that the spectral index of the compact regions (zone 1) is steeper than the diffusion regions (zone 2). However, our calculation results of spectral indices for each scale components show that the diffusion region of large scales components is steeper (see Figure 4). The results are significantly inconsistent with what is predicted in Atoyan et al. (2000b).

To explain the distribution of the spectral index in Figure 4, we consider the following scenario:

(1) The post-shock magnetic field is not a constant field but an exponentially damped field, described by the equation (Pohl et al. 2005; Tran et al. 2015)

$$B(x) = (B_0 - B_{\min})\exp(-x/a_b) + B_{\min}. \quad (2)$$

Here, B_0 represents the magnetic field immediately downstream of the shock, and a_b is the e -folding damping length-scale.

(2) High-energy electrons are accelerated by the forward and reverse shocks and lose their energy as they propagate through the post-shock region via synchrotron radiation and/or inverse Compton scattering. When the propagation distance is less than the damping length-scale the strong magnetic field effectively cools down the GeV electrons through synchrotron radiation, resulting in a gradually softer spectrum from small-scale to large-scale components. Beyond that length-scale the strength of the magnetic field decreases rapidly, and the cooling of the electrons becomes less apparent, leading to a nearly constant spectral index.

We estimate the required value of B_0 using the calculations provided in Longair (2011). The energy losses caused by synchrotron radiation and inverse Compton scattering can be

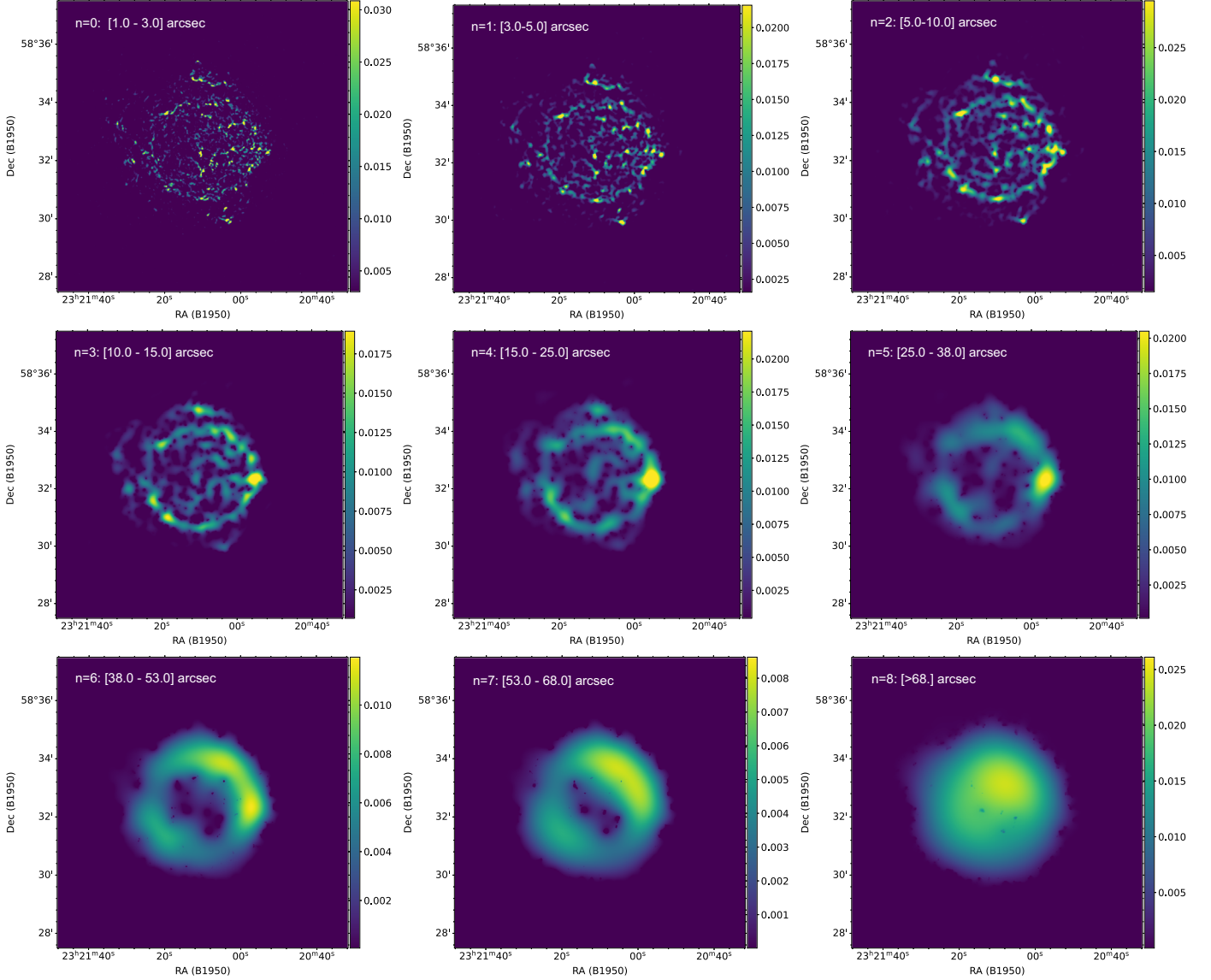


Figure 2. The components of each scale decomposed by CDD. Color-scale is in units of Jy beam⁻¹.

described by the equations:

$$-\left(\frac{dE}{dt}\right)_{\text{synch}} = \frac{4}{3} \sigma_T c \gamma^2 U_{\text{mag}} = 6.6 \times 10^4 \gamma^2 B^2 \quad \text{eV s}^{-2}, \quad (3)$$

$$-\left(\frac{dE}{dt}\right) = \frac{4}{3} \sigma_T c \gamma^2 U_{\text{rad}}. \quad (4)$$

In these equations, σ_T , c , γ , U_{mag} and U_{rad} represent the Thomson cross-section, speed of light in a vacuum, Lorentz factor, magnetic field energy density, and radiation energy density, respectively. For Cas A, the photon fields contributing to inverse Compton scattering are the 2.7 K cosmic microwave

background and the far-infrared field with a value of $\sim 2 \text{ eV cm}^{-3}$ (Ahnen et al. 2017). Assuming the upper limit of the cooling time is the age of Cas A, e.g., 350 yr (Suzuki et al. 2021), we obtain a lower limit of $200 \mu\text{G}$ for the magnetic field B_0 , which is consistent with previous results such as Cowsik & Sarkar (1980), Atoyan et al. (2000a) and Vink & Laming (2003). It is worth noting that the theoretical calculation of the spectral index as a function of the length scale based on the damped-magnetic-field model needs to consider a three-dimensional projection. Because the morphology of Cas A is quite complex, the component scales cannot be described by a simple function. Therefore, we take $15''$ as a typical value of the damping length-scale due to the spectral

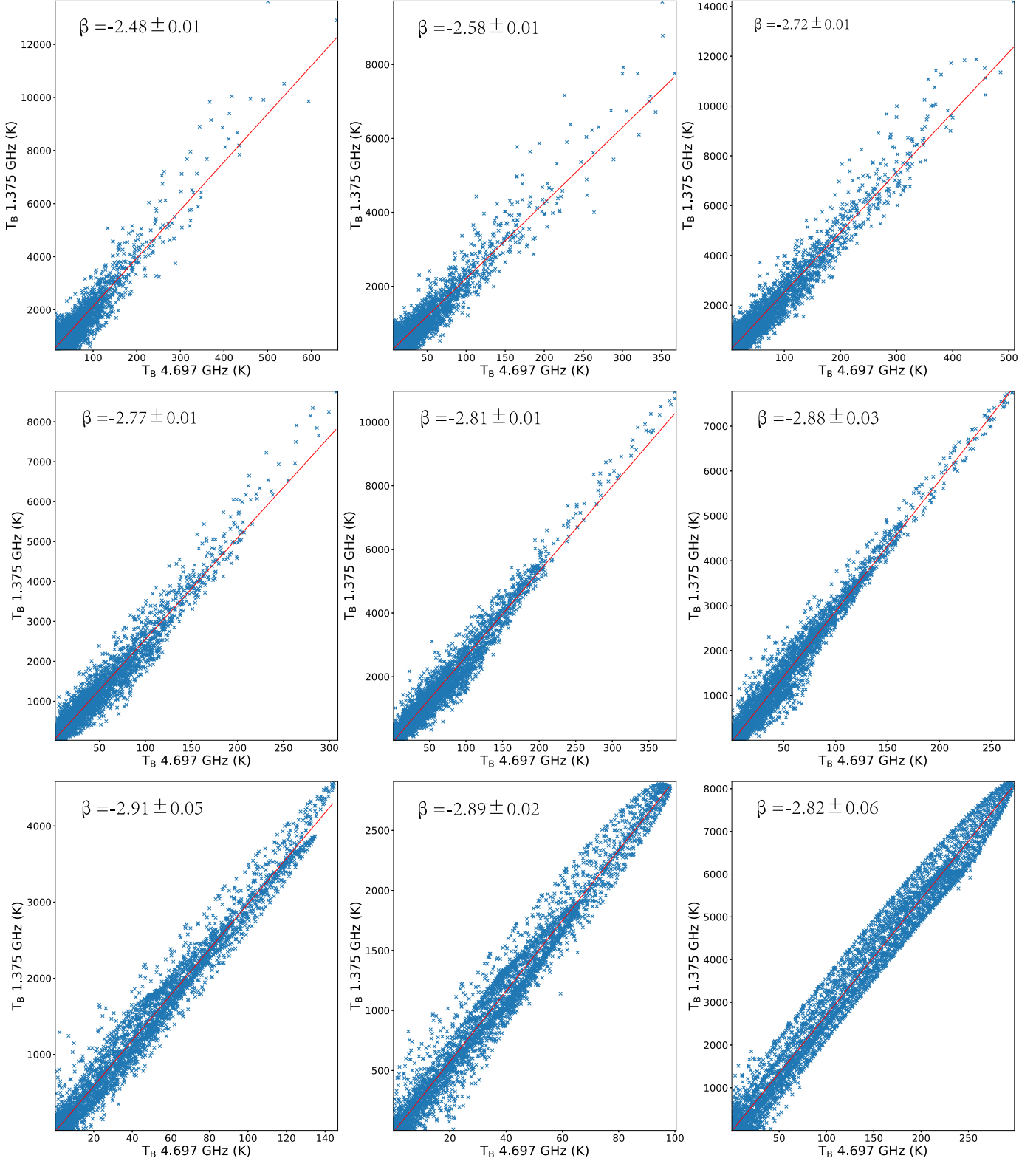


Figure 3. T-T plots for each component of Cas A between 1.475 and 4.747 GHz.

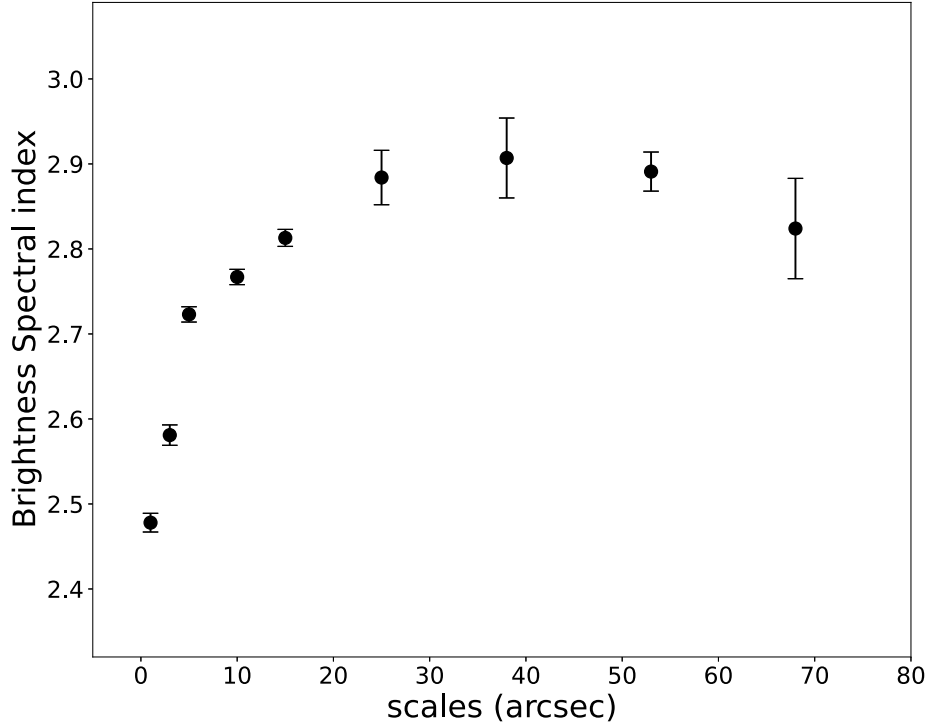


Figure 4. The distribution of the brightness temperature spectral index of each component.

index being flattened after the component scales larger than $15''$. The distance of Cas A is ~ 3.4 kpc, indicating that the damping length-scale is less than 7.4×10^{17} cm corresponding to $\sim 10\%$ of Cas A's radius. This result is also consistent with the theoretical prediction of the thickness of the region with enhanced magnetic field strength, which ranges from 10^{16} to 10^{17} cm (Pohl et al. 2005).

4. Summary

Thanks to the high-resolution observations by VLA of Cas A at 6 cm and 21 cm, this essay is the first time to measure the spectral indices of various scale components in Cas A. The overall mean spectral index is $\alpha = -0.78 \pm 0.02$, and the spectral index of various scale components is in the range of -0.48 ± 0.01 to -0.91 ± 0.05 . The spectral index steepens from small to large scale components, which contradicts the expected spectral index distribution of the two-zone model developed by Atoyan et al. (2000b). To explain these multi-component spectral index distributions, we consider a damped post-shock magnetic field model described by Equation (2). We find that, if the magnetic field immediately downstream of the shock is larger than $\sim 200 \mu\text{G}$ and the damping length-scale is smaller than $\sim 10\%$ of Cas A's radius, the distribution of the spectral index can be accounted for naturally.

Acknowledgments

We thank Dr. Xiaohui Sun, Siming Liu and Aiyuan Yang for their helpful comments when preparing this paper. We acknowledge support from the National Natural Science Foundation of China (NSFC, Grant Nos. 12041301 and 12073039), the China Manned Space Project (CMS-CSST-2021-A09), and the Youth Innovation Promotion Association of CAS (2023000015). We thank the staff of the Karl G. Jansky Very Large Array for their efforts in the observation of Cassiopeia A and data preservation. X.L. and Z.Y. have equal contributions to this paper.

ORCID iDs

Zongyao Yin  <https://orcid.org/0009-0007-7029-4461>

References

- Ackermann, M., Ajello, M., Allafort, A., et al. 2013, *Sci*, **339**, 807
- Aharonian, F., Akhperjanian, A., Barrio, J., et al. 2001, *A&A*, **370**, 112
- Ahnen, M. L., Ansoldi, S., Antonelli, L. A., et al. 2017, *MNRAS*, **472**, 2956
- Albert, J., Aliu, E., Anderhub, H., et al. 2007, *A&A*, **474**, 937
- Anderson, M., Rudnick, L., Leppik, P., et al. 1991, *ApJ*, **373**, 146
- Anderson, M. C., & Rudnick, L. 1995, *ApJ*, **441**, 307
- Anderson, M. C., & Rudnick, L. 1996, *ApJ*, **456**, 234
- Atoyan, A. M., Aharonian, F. A., Tuffs, R. J., et al. 2000a, *A&A*, **355**, 211
- Atoyan, A. M., Tuffs, R. J., Aharonian, F. A., et al. 2000b, *A&A*, **354**, 915
- Baars, J. W. M., Genzel, R., Pauliny-Toth, I. I. K., et al. 1977, *A&A*, **61**, 99
- Bell, A. R. 1978, *MNRAS*, **182**, 147

- Blandford, R., & Eichler, D. 1987, [PhR](#), **154**, 1
- Blasi, P. 2013, [A&ARv](#), **21**, 70
- Brose, R., Sushch, I., & Mackey, J. 2022, [MNRAS](#), **516**, 492
- Cao, Z., Aharonian, F. A., An, Q., et al. 2021, [Natur](#), **594**, 33
- Cardillo, M., Tavani, M., Giuliani, A., et al. 2014, [A&A](#), **565**, A74
- Cornwell, T. J. 2008, [ISTSP](#), **2**, 793
- Cowsik, R., & Sarkar, S. 1980, [MNRAS](#), **191**, 855
- DeLaney, T., Kassim, N. E., Rudnick, L., et al. 2014, [ApJ](#), **785**, 7
- Domček, V., Vink, J., Hernández Santisteban, J. V., et al. 2021, [MNRAS](#), **502**, 1026
- Fesen, R. A., Hammell, M. C., Morse, J., et al. 2006, [ApJ](#), **645**, 283
- Gothelf, E. V., Koralesky, B., Rudnick, L., et al. 2001, [ApJL](#), **552**, L39
- Green, D. A. 2019, [JApA](#), **40**, 36
- Helder, E. A., & Vink, J. 2008, [ApJ](#), **686**, 1094
- Humensky, T. B. 2008, in AIP Conf. Ser. 1085 (Melville, NY: AIP), 357
- Jogler, T., & Funk, S. 2016, [ApJ](#), **816**, 100
- Kassim, N. E., Perley, R. A., Dwarakanath, K. S., et al. 1995, [ApJL](#), **455**, L59
- Krause, O., Birkmann, S. M., Usuda, T., et al. 2008, [Sci](#), **320**, 1195
- Lei, X., Zhu, H., Zhang, H., et al. 2022, [ApJ](#), **941**, 13
- Li, G.-X. 2022, [ApJS](#), **259**, 59
- Longair, M. S. 2011, High Energy Astrophysics (Cambridge: Cambridge Univ. Press), 2011
- McMullin, J. P., Waters, B., Schiebel, D., et al. 2007, [adass XVI](#), **376**, 127
- Morse, J. A., Fesen, R. A., Chevalier, R. A., et al. 2004, [ApJ](#), **614**, 727
- Pohl, M., Yan, H., & Lazarian, A. 2005, [ApJL](#), **626**, L101
- Reed, J. E., Hester, J. J., Fabian, A. C., et al. 1995, [ApJ](#), **440**, 706
- Suzuki, H., Bamba, A., & Shibata, S. 2021, [ApJ](#), **914**, 103
- Tian, W. W., Leahy, D. A., Haverkorn, M., et al. 2008, [ApJL](#), **679**, L85
- Tran, A., Williams, B. J., Petre, R., et al. 2015, [ApJ](#), **812**, 101
- Trotter, A. S., Reichart, D. E., Egger, R. E., et al. 2017, [MNRAS](#), **469**, 1299
- Turtle, A. J., Pugh, J. F., Kenderdine, S., et al. 1962, [MNRAS](#), **124**, 297
- Vink, J., & Bamba, A. 2022, in Handbook of X-ray and Gamma-ray Astrophysics Cosimo Bambi and Andrea Santangeloed. C. Bambi & A. Santangelo (Berlin: Springer)
- Vink, J., & Laming, J. M. 2003, [ApJ](#), **584**, 758
- Wright, M., Dickel, J., Koralesky, B., et al. 1999, [ApJ](#), **518**, 284